Dalton Transactions

ROYAL SOCIETY OF CHEMISTRY

PAPER

View Article Online
View Journal | View Issue

Cite this: *Dalton Trans.*, 2025, **54**, 8510

Electronic structure of molybdenum chalcogenide clusters as supports for low-valent actinides†

Pere Miró *[a,b] and S. Genevieve Duggan [a,b]

The metallation, bonding, and electronic structure of redox active incomplete-cubane $M_3(\mu_3\text{-}Q)(\mu_2\text{-}Q)_3$ chalcogenide clusters with early actinides were studied using density functional theory and multireference methodologies. We confirmed that the incorporation of low-valent U(III) leads to its oxidation to U(IV) due to an intramolecular redox reaction with the molybdenum sulfide core. On the contrary, open questions remain with respect to the oxidation state of low-valent transuranic elements upon their coordination to the molybdenum sulfide core. Density functional theory calculations indicate that the transuranic center remains An(III), while complete active space calculations suggest an actinide oxidation analogous to the one observed in the uranium species. The predominantly electrostatic bonding between the actinides and the molybdenum sulfide cluster was assigned using the quantum theory of atoms in molecules. Our results on clusters with harder and softer chalcogenides are in agreement with a preferential soft–soft interaction between the actinide and its support.

Received 18th October 2024,
Accepted 9th April 2025

DOI: 10.1039/d4dt02911a

rsc.li/dalton

1 Introduction

In the last decade, layered transition-metal chalcogenides (TMC) have rapidly emerged for spintronics, optoelectronics, energy harvesting, and flexible electronics applications as they display unique chemical and physical properties that are absent or difficult to obtain in other materials.[1–3] The relatively weak van der Waals interaction between TMC layers allows for the intercalation of ions to tune the electronic properties of these materials which can be also used for chemical separations.[4] In this aspect, molybdenum disulfide (MoS_2) has been used to extract uranium from sea water, taking advantage of the soft–soft interactions between uranium and the chalcogenide surface to preferentially uptake uranium over harder ions.[5,6] For uranium, the aqueous solution is dominated by the hexavalent state in the form of the uranyl ion. Under reducing conditions, uranium forms tetravalent U(IV) species, which are significantly less soluble in aqueous media than hexavalent U(VI) ones. Tang *et al.* reduced uranium to enhance its extraction with MoS_2 *via* the formation of unstable pentavalent U(V) species which disproportionate back to U(VI) and U(IV) phases.[7] Other actinides such as thorium(IV) have been extracted using MoS_2, opening up the possibility of exploring TMC surfaces for separations of other actinide species.[8] Therefore, it is important to understand the nature of the interaction of reduced actinide ions with chalcogenide surfaces to improve actinide separations based on TMC as well as to develop new ones.

Incomplete-cubane transition metal chalcogenide clusters, such as Mo_3S_4, can be used as redox active molecular analogues of TMC surfaces.[9–11] Many incomplete-cubane TMC clusters containing M_3Q_4 cores (Q = O, S, Se, or Te) have been isolated for both molybdenum and tungsten.[12–14] Incorporation of a second metal into the these cores leads to cubane-like heterobimetallic clusters.[15–17] Recently, Matson and co-workers[10,11] incorporated for the first time, an actinide center into the $[(Cp^*)_3Mo_3S_4]$ species through its reaction with $[(Cp^*)U(III)(I)_2(THF)_3]$. Based on the X-Ray diffraction of this species, the authors suggested that coordination of the U(III) center to the Mo_3S_4 core induces an intramolecular redox reaction forming $[(Cp^*)_3Mo_3S_4][U(IV)(Cp^*)(I)_2]$. Upon the addition of 2.2 equivalents of KC_8, the Mo_3S_4 core is fully reduced with three Mo(III) centers. Finally, the addition of an additional 2.2 equivalents of KC_8 was proposed to lead to the reduction of the actinide center. The formation of a low-valent uranium species was inferred *via* its reactivity with azobenzene, and they are assigned as the synthetic equivalent to an U(II) species.[18]

Herein, we investigate the electronic structure, chemical bonding, and electrochemical properties of molybdenum chalcogenide clusters metalated with low-valent actinides. Specifically, we explored the impact of the actinide's nature by

[a]*Department of Chemistry, University of Iowa, Iowa City, IA 52242, USA. E-mail: pere-miro@uiowa.edu*
[b]*Department of Chemistry, University of South Dakota, Vermillion, SD 57069, USA. E-mail: pere.miro@usd.edu*

†Electronic supplementary information (ESI) available: Spin density, CASSCF active space, All calculations are available in the ioChem-BD repository. See DOI: https://doi.org/10.1039/d4dt02911a

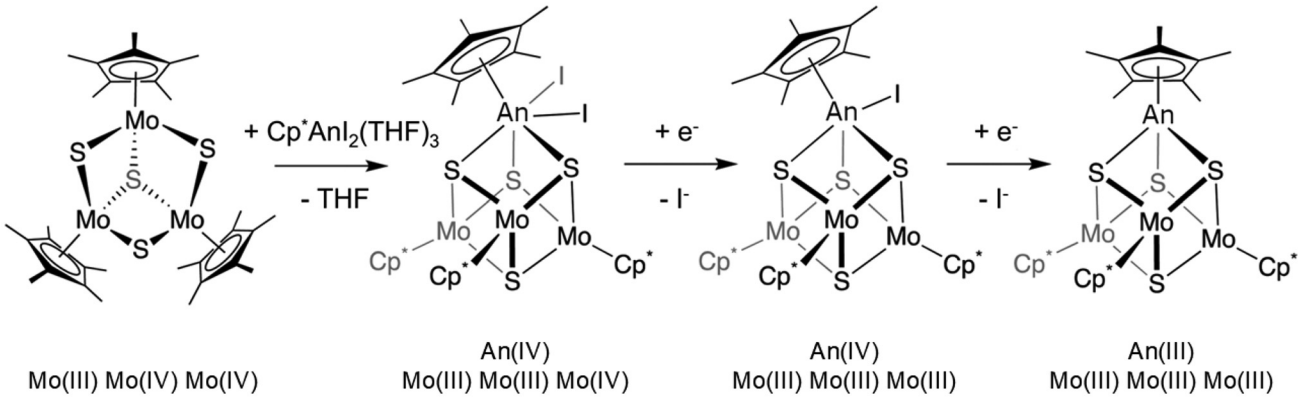

Fig. 1 Species involved in the actinide metallation of $[(Cp^*)_3Mo_3S_4]$ and its derived species. From left to right: unmetalated $[(Cp^*)_3Mo_3S_4]$ and metalated $[(Cp^*)_3Mo_3S_4][An(Cp^*)(I)_2]$, $[(Cp^*)_3Mo_3S_4][An(Cp^*)(I)]$, and $[(Cp^*)_3Mo_3S_4][An(Cp^*)]$. Formal oxidation states of the molybdenum and actinide center are shown below each species.

expanding upon the experimentally isolated uranium $[(Cp^*)_3Mo_3S_4][U(Cp^*)(I)_2]$ and derived species to include transuranic elements (Fig. 1). Furthermore, we also investigated the effect of the TMC support by studying both harder and softer chalcogenides.

2 Computational details

Density Functional Theory (DFT) calculations were performed using the Amsterdam Density Functional package with the PBE exchange–correlation functional in conjunction with a triple-ζ Slater-type basis set with a small frozen core and an additional polarization function.[19–22] Relativistic corrections were taken into account using the scalar relativistic zero-order regular approximation (ZORA).[23] All species with unpaired electrons were considered to be in their high spin state indicating the highest possible multiplicity between the actinide 5f electrons and any unpaired 4d molybdenum electrons. Dispersion effects were included using Grimme's D3 correction.[24] The nature of all stationary points and transition states were verified by the calculation of analytical vibrational frequencies. Single point calculations on the gas phase optimized geometries were performed with the hybrid PBE0 exchange–correlation functional in conjunction with an all electron triple-ζ Slater-type basis set with an additional polarization function. Solvent effects were included in the PBE0-D3/TZP single point calculations using the COSMO solvation model with toluene parameters on gas phase optimized geometries at the PBE/TZP level of theory.[25–27] All calculations were performed without symmetry constraints. Redox potentials were calculated with respect to the ferricenium/ferrocene (Fc^+/Fc) reference electrode in non-aqueous media.[28,29]

Multiconfigurational complete active space self-consistent field (CASSCF) calculations followed by second-order perturbation theory (CASPT2) were performed on the DFT optimized geometries using the OpenMolcas software suite.[30–32] For the fully reduced unmetallated species, an active space of 9 electrons in 9 orbitals (9e, 9o) was used. This includes the three lowest 4d orbitals for each of the molybdenum centers and all the corresponding electrons. This choice is based on the crystal field splitting expected for the three quasi C_{3v} molybdenum centers. Each center has a symmetric ligand environment that will lead to a large crystal field splitting. An analogous active space was used for the singly and doubly reduced species with (7e, 9o) and (8e, 9o) active spaces, respectively. For uranium species, we used an (Xe, 16o) active space that included all the uranium f electrons distributed in the seven 5f orbitals, and the three lowest 4d orbitals for each of the molybdenum centers (X = 10, 11, and 12 for $[(Cp^*)_3Mo_3S_4][U(Cp^*)(I)_2]$, $[(Cp^*)_3Mo_3S_4][U(Cp^*)(I)]$, and $[(Cp^*)_3Mo_3S_4][U(Cp^*)]$, respectively). Analogous calculations were performed for the neptunium and plutonium species.[33] The resulting active natural orbitals are presented in the ESI (Fig. S8–S14†). For CASPT2 calculations, an imaginary shift of 0.2 au and the so-called IPEA shift of 0.25 were employed.[33,34] Scalar relativistic effects were included at the CASSCF level using the second order Douglas–Kroll–Hess Hamiltonian and relativistic all electron ANO-RCC basis sets.[35–38] Specifically, the following contractions were used: [9s,8p,6d,4f,2g,1h] for uranium, neptunium, and plutonium, [7s,6p,4d,2f,1g] for molybdenum, [6s,5p,3d,1f] for iodine, [4s,3p,1d] for sulfur, [3s,2p,1d] for carbon atoms coordinated to molybdenum or actinide centers, [2s,1p] for all other carbon atoms, and [1s] for hydrogen. Cholesky decomposition in conjunction with local-exchange screening was used to reduce the computational cost.[39] For CASPT2 calculations, the default number of frozen orbitals was selected in the correlation space. We also explored the performance of multiconfiguration pair-density functional theory (MC-PDFT) with a translated PBE functional as a less computationally expensive alternative to recover dynamic correlation than second-order perturbation theory.[40] For the systems in this study, spin splitting energies from MC-PDFT are in good agreement with CASPT2; however, this is system-dependent and should always be tested.

3 Results and discussion

3.1 Unmetallated molybdenum sulfide clusters

Incomplete cubane-type clusters with both molybdenum oxide (Mo_3O_4) and sulfide cores (Mo_3S_4) have been experimentally isolated with different capping ligands. Similarly, many incomplete cubane-type clusters with $Mo_3O_{4-n}S_n$ cores have been synthesized, and their structures have been determined by single crystal X-ray diffraction. Molybdenum is in oxidation state IV in these species; however, one can easily reduce these centers to oxidation state III. For example, both $[(Cp^*)_3Mo_3S_4]PF_6$ and $[(Cp^*)_3Mo_3S_4]$ complexes have been isolated, having a formally Mo(III)Mo(VI)$_2$ oxidation state.[41] The former species is diamagnetic with three metal–metal bonded Mo(IV) (d^2) centers, while the latter has a single unpaired electron. Our density functional theory optimized geometry for $[(Cp^*)_3Mo_3S_4]^+$ has molybdenum–molybdenum, molybdenum–sulfur (μ_2), and molybdenum–sulfur (μ_3) distances of *ca.* 2.83 Å, 2.31 Å, and 2.35 Å, respectively. The first reduction of this unmetallated cluster from the all Mo(IV) species is localized, generating a single Mo(III) center, as shown by the localized spin density on a single molybdenum center (Fig. 2 left).

This can be explained since even though the Cp* ligands break the symmetry of the Mo_3S_4 core, it maintains quasi C_s symmetry where the two quasi-equivalent molybdenum centers remain in oxidation state IV, while the remaining one is reduced. A second reduction to generate a formally Mo(IV)Mo(III)$_2$ species leads to a triplet ground state with delocalized redox states between the molybdenum centers thus the oxidation state of this cluster would be better described using Enemark–Feltham notation $\{Mo(IV)_3\}^2$ (Fig. 2 right).[42] In this notation it is clear that we have three centers with 2 d electrons each but an additional 2 electrons are delocalized between the three molybdenum centers. Finally, the third reduction generates an all Mo(III) species with similar spin density on all three molybdenum centers and a quartet ground state (Table S3†). In all of these species, the bridging sulfide centers have a small fraction of the spin density that increases as the formal number of Mo(III) centers increases. The μ_3 sulfide ligand has a lower spin density than the μ_2 sulfide ligands until the third reduction. The calculated redox potentials for the first reduction of the $[Mo_3S_4Cp_3^*]$ species is −1.34 V with respect to the Fc/Fc^+ reference electrode, which is in very good agreement with the experimental reduction of these species (−1.26 V in toluene). The second calculated reduction potential is −3.25 V which is significantly lower than the experimental value. We attribute this to other interactions present in experiment that facilitate this redox event not being captured by our calculations such as ion pairing in the $[Mo_3S_4Cp_3^*]$ species with alkali cations and a crown ether.[43]

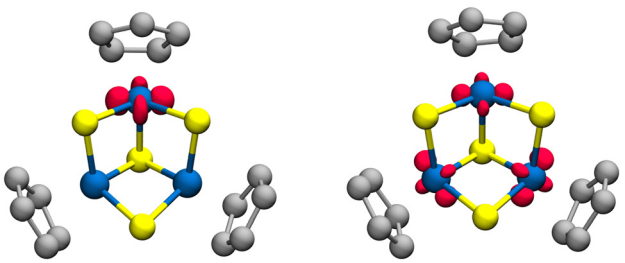

Fig. 2 Spin density for the unmetalated $[(Cp^*)_3Mo_3S_4]$ (left) and $[(Cp^*)_3Mo_3S_4]^-$ (right) clusters at PBE0/TZP/COSMO level of theory. Spin density isovalue was set to 0.03. Methyl groups in Cp* ligands are not shown for clarity. Color code: molybdenum in blue, sulfur in yellow, carbon in grey, hydrogen in white, and spin density in red.

The complete active space calculations (CASPT2) confirm doublet, triplet, and quartet ground states for the $[(Cp^*)_3Mo_3S_4]$, $[(Cp^*)_3Mo_3S_4]^-$, and $[(Cp^*)_3Mo_3S_4]^{2-}$ species, respectively. However, the Mo(III) centers in the doubly reduced species are localized in CASSCF (Table S4†), suggesting density functional theory could be overdelocalizing the spin in these species. Some multiconfigurational character is observed arising from contributions of electron configurations associated with partial occupation of anti-bonding orbitals in the Mo–Mo bonds, a common occurrence in metal–metal bonding.[44]

3.2 Thorium molybdenum sulfide clusters

We decided to first study the addition of Th(IV) to the cluster as a non-redox active actinide. We assumed the formation of $[(Cp^*)_3Mo_3S_4][Th(IV)(Cp^*)(I)_2]^+$ could be the analog to $[(Cp^*)_3Mo_3S_4][U(IV)(Cp^*)(I)_2]$ isolated by Matson and co-workers.[10] The thorium metallation cannot involve an intramolecular redox reaction between thorium and the Mo_3S_4 core due to the inaccessibility of lower oxidation states for thorium under the same experimental conditions used in the synthesis of $[(Cp^*)_3Mo_3S_4][U(Cp^*)(I)_2]$.[10] Any reduction of the $[(Cp^*)_3Mo_3S_4][Th(Cp^*)(I)_2]^+$ species must add electrons into the Mo_3S_4 core. In contrast with the unmetallated species, all the reductions of $[(Cp^*)_3Mo_3S_4][Th(Cp^*)(I)_2]^+$ lead to localized Mo(III) centers (Table S11†). This can be attributed to the more asymmetric environment in metallated species due to the presence of the additional Cp* and two iodide ligands in the thorium coordination sphere as we assumed no iodide was decoordinated upon cluster reduction. Furthermore, the thorium center coordinates to the Mo_3S_4 support *via* three μ_2-S ligands, reducing their spin densities with respect to the unmetallated species (Table S3 *cf.* Table S11†).

3.3 Uranium and transuranic metallation of molybdenum chalcogenide clusters

Experimentally, Matson and co-workers[10] used $[(Cp^*)U(I)_2(THF)_3]$ as their metallating agent; however, exactly analogous species with neptunium and plutonium do not exist. Nevertheless, similar species with two Cp* ligands, $[(Cp^*)_2An(I)(THF)]$, exist for neptunium and plutonium.[45] Alternative species without the Cp* such as $[An(I)_3(THF)_4]$ have been isolated for all three actinides.[46] Therefore, we decided to explore the metallation of $[(Cp^*)_3Mo_3S_4]$ by keeping the metallating species as $[(Cp^*)An(I)_2(THF)_3]$ for all three actinides. This allows us to focus on the differences arising from the acti-

Table 1 Enthalpies and Gibbs free energies (in parenthesis) for the metallation of the $[(Cp^*)_3Mo_3Q_4]$ molybdenum chalcogenide clusters (where Q = O, S, or Se.). Energies in kcal mol^{-1}

	O	S	Se
U	−5.5 (−23.0)	−13.3 (−32.9)	−14.2 (−31.9)
Np	−0.5 (−18.9)	+3.0 (−17.5)	+0.7 (−17.7)
Pu	+13.0 (−5.9)	+2.0 (−18.1)	+0.1 (−18.3)

nide's nature, rather than the metallating species. The enthalpies and Gibbs free energies of metallation of the molybdenum chalcogenide clusters are presented in Table 1.

While the metallation of all molybdenum sulfide clusters are exergonic independent of the actinide (U, Np, or Pu), it is significantly more favorable to incorporate uranium than transuranic elements. The entropic effects at room temperature contribute *ca.* −19 kcal mol^{-1} and are linked to the decoordination of the tetrahydrofuran ligands in $[(Cp^*)An(I)_2(THF)_3]$. As expected the entropic contribution to the metallation Gibbs free energy is actinide independent as such a dependence is part of the metallation enthalpy. In contrast to the free energies, not all of the reactions are enthalpically favorable (*i.e.*, not all reactions are exothermic). The experimentally isolated structure for $[(Cp^*)_3Mo_3S_4][U(Cp^*)(I)_2]$ indicated that the coordination of U(III) to the molybdenum sulfide cluster involved an intramolecular redox reaction leading to species with Mo(III)$_2$Mo(IV)U(IV) formal oxidation states.[10] All species have frontier molecular orbitals with significant orbital delocalization between the $[Mo_3S_4]$ core and the actinide thus rendering any oxidation state assignment challenging (Fig. S5–S7†). Nevertheless, the spin densities of $[(Cp^*)_3Mo_3S_4][An(Cp^*)(I)_2]$ and $[(Cp^*)_3Mo_3S_4][An(Cp^*)(I)]$ are presented in Fig. 3 and Table 2. The oxidation of U(III) to U(IV) can be assessed by the drop in spin density of the uranium center from the precursor to the $[(Cp^*)_3Mo_3S_4][U(Cp^*)(I)_2]$ species (2.24 *cf.* 2.95). On the other hand, the neptunium and plutonium metallation show a significantly lower change in the spin density at the actinide (3.73 *cf.* 4.00 for neptunium and 4.98 *cf.* 5.05 for plutonium). This is in agreement with the U(IV)/U(III) redox potential being lower than in the transuranic counterparts.[47] DFT calculations suggest that the transuranic elements could remain in their low-valent state upon their incorporation to the $[(Cp^*)_3Mo_3S_4]$ species. Additionally, the two Mo(III) centers in $[(Cp^*)_3Mo_3S_4][U(Cp^*)(I)_2]$ are delocalized, which is in agreement with a $\{Mo(IV)_3\}^2$ U(IV) oxidation state. On the contrary, the $[(Cp^*)_3Mo_3S_4][Pu(Cp^*)(I)_2]$ species present with a single localized Mo(III) center which would be in agreement with a Mo(III)Mo(IV)$_2$Pu(III) oxidation state assignment (Table 2). Finally, no clear oxidation state can be assigned from DFT in the neptunium complex due to spin delocalization.

Metal–ligand interactions are dictated by the hard–soft acid–base principle, whereby soft low-valent actinides interact most strongly with soft chalcogenides and *vice versa*. Therefore, we studied the metallation of $[(Cp^*)_3Mo_3O_4]$ and $[(Cp^*)_3Mo_3Se_4]$ species which contain harder and softer chalcogenides (Table 1). These metallations follow the same trend as those observed in the sulfide species with respect to the actinide nature. The hard–soft acid–base principle between the actinide and the different chalcogenides reveals a preferential binding with softer surfaces (Table 1). The uranium metallation Gibbs free energy of molybdenum oxide, sulfide, and selenide substrates are −23.0, −32.9, and −31.9 kcal mol^{-1} respectively, following the trend in chemical hardness of oxygen with respect to sulphur and selenium.[48]

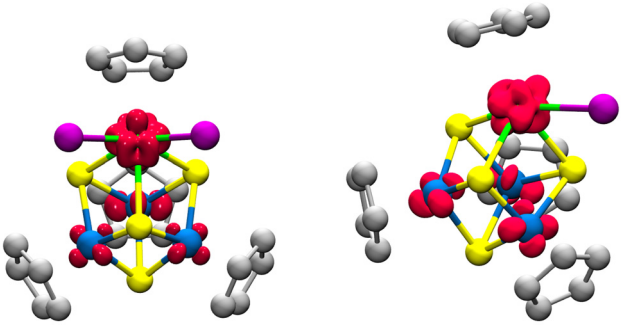

Fig. 3 Spin density for the $[(Cp^*)_3Mo_3S_4][U(Cp^*)(I)_2]$ (left) and $[(Cp^*)_3Mo_3S_4][U(Cp^*)(I)]$ (right) species at PBE0/TZP/COSMO level of theory. Spin density isovalue was set to 0.03. Methyl groups in Cp* ligands are not shown for clarity. Color code: uranium in green, molybdenum in blue, sulfur in yellow, carbon in grey, hydrogen in white, and spin density in red.

Table 2 Ground state DFT Bader spin densities for the $[(Cp^*)_3Mo_3S_4][An(Cp^*)(I)_2]$ and $[(Cp^*)_3Mo_3S_4][An(Cp^*)(I)]$ species (ground state CASSCF Mulliken spin densities in parenthesis)

Species	An	Mo(1)	Mo(2)	Mo(3)
$[(Cp^*)_3Mo_3S_4][U(Cp^*)(I)_2]$	2.24(2.00)	0.52(0.89)	0.48(−0.03)	0.79(0.94)
$[(Cp^*)_3Mo_3S_4][Np(Cp^*)(I)_2]$	3.73(2.99)	0.65(0.87)	0.65(−0.04)	−0.08(0.96)
$[(Cp^*)_3Mo_3S_4][Pu(Cp^*)(I)_2]$	4.98(3.99)	0.12(0.85)	0.03(0.00)	0.89(0.94)
$[(Cp^*)_3Mo_3S_4][U(Cp^*)(I)]$	2.47(2.07)	0.78(0.89)	0.68(0.89)	0.80(0.85)
$[(Cp^*)_3Mo_3S_4][Np(Cp^*)(I)]$	3.81(3.08)	0.71(0.87)	0.51(0.88)	0.83(0.86)
$[(Cp^*)_3Mo_3S_4][Pu(Cp^*)(I)]$	5.07(4.07)	0.77(0.88)	0.21(0.87)	0.85(0.86)

Multiconfigurational CASPT2 calculations on $[(Cp^*)_3Mo_3S_4][U(Cp^*)(I)_2]$ species confirmed a high spin quintet ground state, which arises from the ferromagnetic coupling between the two uranium f electrons and the two $[Mo_3S_4]$ core d electrons (Table 3). The antiferromagnetic singlet state is 1.3 kcal mol^{-1} higher in energy, suggesting a weak coupling between the uranium and the Mo_3S_4 core. Finally a triplet state involving antiferromagnetic coupling of the two Mo_3S_4 electrons is 2.8 kcal mol^{-1} higher than the ground state. MC-PDFT calculated splittings are in agreement with CASPT2, thus validating this methodology for the study of actinide systems herein. Similar results were obtained *via* MC-PDFT for the $[(Cp^*)_3Mo_3S_4][An(Cp^*)(I)_2]$ species with neptunium and plutonium. Specifically, the neptunium species have an antiferromagnetic doublet ground state while the ferromagnetic sextet state is less than 1 kcal mol^{-1} higher in

Table 3 Energy splitting at CASPT2 and MC-PDFT levels of theory for the $[(Cp^*)_3Mo_3S_4][U(Cp^*)(I)_2]$ species and their dominant CASSCF configurations. Only configurations with more than 10% weight are considered dominant. Bold occupations are predominantly 4d orbitals in molybdenum. Occupations are labeled as 2 (doubly occupied), u (unpaired up), d (unpaired down), and 0 (unoccupied). Energies in kcal mol^{-1}. See ESI† for CASSCF orbitals and configuration averaged occupations

State	CASPT2	MC-PDFT	Weight	Configuration
Quintet	0.0	0.0	59.6%	**222**u0000u0**0uu000**
			15.1%	**2220**u0u0000**uu000**
Triplet	2.8	2.0	29.3%	**222**u0000u0**002000**
			28.2%	**222**u0000u0**020000**
Singlet	1.3	1.0	43.1%	**222**u0000u0**0dd000**
			12.6%	**2220**u0u0000**dd000**

energy (Table S18†). In the plutonium species, the ferromagnetic septet and antiferromagnetic triplet states are degenerate (Table S20†). This indicates that the coupling between the actinide and Mo_3S_4 core weakens across the actinide series. The natural orbitals are localized either on the actinide or the $[Mo_3S_4]$ cluster allowing us to assign a Mo(III)$_2$Mo(IV)An (IV) oxidation states, which is further supported by the Mulliken atomic spin densities (Table 2 and Fig. S8, S11, and S13†).

3.4 Reduction of actinide molybdenum chalcogenide clusters

Experimentally, the reduction of $[(Cp^*)_3Mo_3S_4][U(Cp^*)(I)_2]$ using 2.2 equivalents of KC_8 is followed by the decoordination of an iodide, which leads to the generation of $[(Cp^*)_3Mo_3S_4][U(Cp^*)]$ species. The changes in spin density upon reduction take place predominantly in the molybdenum centers especially for transuranic species (Table 2). This is in agreement with a reduction event taking place in the Mo_3S_4 core. Furthermore, the calculated vertical electron affinities for this redox event are −2.72, −2.89, and −2.79 eV for the uranium, neptunium, and plutonium species respectively. The vertical electron affinities are very similar for all the actinide species further supporting that this event takes place at the molybdenum centers. Multiconfigurational MC-PDFT calculations confirmed a high spin ground state for all $[(Cp^*)_3Mo_3S_4][An(Cp^*)(I)]$ species with low lying excited states, each with the expected varying degrees of antiferromagnetic coupling character (Tables S15, S18, and S20†). No mixing between either uranium- or plutonium-based orbitals is observed indicating a Mo(III)$_3$An(IV) oxidation state profile. Two singly occupied natural orbitals show mixing between neptunium and molybdenum; however, the Mulliken spin density supports the assignment of Mo(III)$_3$Np(IV) as well. Note that the experimental $[(Cp^*)_3Mo_3S_4][U(Cp^*)(I)]$ crystal structure presents with two Mo–Mo distances of *ca.* 2.896 Å and a short one of 2.676 Å, while all of the Mo–Mo distances in the DFT structure are *ca.* 2.906 Å (Table S13†). The experimental spectroscopic data of these species suggest a symmetric $[Mo_3S_4]$ environment in solution.[10] Geometry optimizations with other spin states result in a shorter Mo–Mo distance of 2.787 Å with the remaining ones *ca.* 2.899 Å; however, they contain significant spin contamination (Table S10†). Additionally, no sign of bond formation is present in the CASSCF calculations; therefore, we hypothesize the origin of the experimentally observed shorter Mo–Mo distance is due to solid state effects.

The final reduction of $[(Cp^*)_3Mo_3S_4][U(Cp^*)(I)]$ and the decoordination of an iodide leads to the generation of $[(Cp^*)_3Mo_3S_4][U(Cp^*)]$ species with three Mo(III) and one U(III) center. Since these species have not been experimentally isolated but inferred *via* their reactivity with azobenzene[10] and the discrepancy in the oxidation state of transuranic species between the DFT and CASSCF levels of theory, we limited our study to the uranium species. $[(Cp^*)_3Mo_3S_4][U(Cp^*)]$ species exhibit a more complex electronic structure since the molybdenum centers engage in further Mo(III)–Mo(III) interactions as well as additional coupling with the actinide center. On one hand, DFT predicts a quintet ground state for the $[(Cp^*)_3Mo_3S_4][U(Cp^*)]$ species. On the other hand, CASPT2 predicts a highly multireference triplet ground state with a quintet state just 1.9 kcal mol^{-1} higher in energy (Table S16†). The ground state involves a Mo(III)–Mo(III) interaction and antiferromagnetic coupling of the remaining Mo(III) and the U(III) center, while the low-lying excited state involves ferromagnetic Mo(III)–U(III) interaction. Other spin states lie *ca.* 17 kcal mol^{-1} above the ground state.

3.5 Topological analysis of the electron density

To further characterize the actinide bonding with the molybdenum chalcogenide cluster, we applied quantum theory of atoms in molecules (QTAIM) and analyzed the topology of the electron density. Table 4 contains selected QTAIM descriptors for the actinide–sulfur interaction in $[(Cp^*)_3Mo_3S_4](AnCp^*I_2)$.

In QTAIM, a bond critical point (BCP) exists when there is a saddle point of electron density between two nuclei with a maximum of the electron density in two directions of space and a minimum in the third one. Furthermore, the Laplacian at a BCP, $\nabla^2\rho_b$, is the sum of two negative and one positive eigenvalues of the density Hessian matrix, and thus may be positive or negative. We found a BCP between the actinide and each of the sulfur atoms with $\rho_b < 0.1$ a.u. and a $\nabla^2\rho_b > 0$, which is indicative a closed-shell interaction. The total electronic energy density at the BCP (H_b) is the sum of the kinetic (G_b) and the potential (V_b) energy densities. The former dominates in non-covalent interactions, while the later is associated with accumulation of charge between the nuclei thus dominates in covalent interactions. In all cases, H_b is slightly nega-

Table 4 Selected QTAIM data for actinide and sulfur interaction in the ground state $[(Cp^*)_3Mo_3S_4][An(Cp^*)(I)_2]$ species

	U	Np	Pu
ρ_b	0.055	0.047	0.043
$\nabla^2\rho_b$	0.098	0.098	0.101
H_b	−0.015	−0.010	−0.007
$\lvert V_b\rvert/G_b$	1.378	1.281	1.216
δ(An,S)	0.547	0.465	0.392

tive but very close to zero. Hence, ρ_{BCP}, $\nabla^2\rho_b$, and H_b indicate an ionic type or donor–acceptor interaction with a very small covalent component, in accordance with previous QTAIM analysis on actinide complexes.[49,50] Bianchi and co-workers suggested a bond classification according to the ratio of the potential energy density to the kinetic energy density at the BCP ($|V_b|/G_b$).[51] Clear closed-shell ionic bonds or van der Waals interactions have $|V_b|/G_b < 1$ while clear electron-shared covalent bonds have $|V_b|/G_b > 2$. All actinide–sulfur interactions have $|V_b|/G_b$ of *ca.* 1.35 indicating some covalent contribution.[52] Finally the magnitude of the exchange of electrons between the actinide basin and sulfur basin can be estimated by the delocalization index δ(An,S).[50] If we consider a bonded interaction between the actinide and the sulfur atoms, δ(An,S) can be used as a measure of the bond order between them. These indices decrease along the actinide series indicating a weaker interaction between the actinide and the cluster. The delocalization indices are similar to the ones observed in other predominantly electrostatic actinide bonds.[49,50]

The delocalization index is also used as a metric for energy degeneracy-driven covalency, while the electron density, Laplacian, energy density at the BCP are indicative of overlap-driven covalency. However, it is important to stress that covalency is not a physically observable property and quantifying it *via* QTAIM in actinide bonding is only meaningful when comparing bond covalency changes across different species. That said, the values herein support both higher orbital and degeneracy driven covalency for uranium than for transuranic elements. For the studied species, we observe that all QTAIM descriptors indicate a prevalent actinide–sulfur close-shell interaction with a progressive reduction of small covalent character as we move across the actinide series. Similar conclusions can be drawn from QTAIM analysis of [(Cp*)$_3$Mo$_3$S$_4$][An(Cp*)(I)] (Tables S13†).

4 Conclusions

We studied the metallation, bonding, and electronic structure of redox active incomplete-cubane M_3 (μ_3-Q)(μ_2-Q)$_3$ chalcogenide clusters with low-valent actinides using density functional theory and multireference methodologies. We confirmed that the incorporation of low-valent U(III) to the Mo_3S_4 core leads to species with U(IV) due to an intramolecular redox reaction with the molybdenum sulfide core. $\{Mo(IV)_3\}^2U(IV)$ and $Mo(III)_2Mo(IV)U(IV)$ redox states can be assigned to the [(Cp*)$_3$Mo$_3$S$_4$][U(Cp*)(I)$_2$] species at the DFT and CASSCF levels of theory. For transuranic analogs, density functional theory indicates that the transuranic center remains as an An(III); however, it could be underestimating the charge transfer between the transuranic center and the molybdenum sulfide cluster. Based on spin density, a Mo(III)Mo(IV)Mo(IV)Pu(III) redox state can be assigned to [(Cp*)$_3$Mo$_3$S$_4$][Pu(Cp*)(I)$_2$] species, while no clear redox state assignment can be made for the neptunium analog. On the other hand, complete active space calculations indicate an actinide oxidation analogous to the one observed in the uranium species, thus a $Mo(III)_2Mo(IV)An(IV)$ redox state can be assigned to all [(Cp*)$_3$Mo$_3$S$_4$][An(Cp*)(I)$_2$] species. With CASSCF, the redox state of all derived [(Cp*)$_3$Mo$_3$S$_4$][An(Cp*)(I)] species are better described as $Mo(III)_3An(IV)$. Further experiments are needed to shed light onto the transuranic elements' oxidation state upon their coordination to the [(Cp*)$_3$M$_3$S$_4$] clusters. However, the subtle changes as a function of actinide and ligand choice suggest opportunities to modulate the reactivity and properties of such clusters *via* ligand design.

The predominantly electrostatic bonding between the actinide and the molybdenum sulfide cluster was confirmed using quantum theory of atoms in molecules. Our results on clusters with harder and softer chalcogenides are in agreement with a preferential soft–soft interaction between the actinide and the support. The intrinsic differences in the Gibbs free energies of metallation across the actinides could be exploited in actinide separations approaches; however, the An(III) oxidation state is not common during in current separations. Therefore, further studies are needed to determine if these differences are also present in higher oxidation states such as An(IV).

Author Contributions

P. M. performed the density functional theory and multiconfigurational calculations for the molybdenum sulfide species and directed the research project. S. G. D. performed the QTAIM analysis. The manuscript was written through contributions of all authors, and all authors have given approval of the final version of the manuscript.

Data availability

The data generated for this article will be made available

The computational data for this article, including inputs and outputs are available in an ioChem-BD repository. **https://doi.org/10.19061/iochem-bd-6-412**.

Additional data supporting this article such as frontier orbitals, CASSCF active space details, relative energy of different spin states, and spin densities among others have been included as part of the ESI.†

Conflicts of interest

There are no conflicts to declare.

Acknowledgements

Calculations supporting this project were performed on high-performance computing systems at the University of South Dakota funded by NSF MRI award OAC-1626516. P. M. thanks Prof. Bess Vlaisavljevich for scientific discussions regarding the multireference calculations.

References

1 P. Miró, M. Audiffred and T. Heine, *Coord. Chem. Rev.*, 2014, **43**, 6537–6554.
2 S. Manzeli, D. Ovchinnikov, D. Pasquier, O. Yazyev and A. Kis, *Nat. Rev. Mater.*, 2017, **2**, 17033.
3 H. S. Nalwa, *RSC Adv.*, 2020, **10**, 30529–30602.
4 F. Xiong, H. Wang, X. Liu, J. Sun, M. Brongersma, E. Pop and Y. Cui, *Nano Lett.*, 2015, **15**, 6777–6784.
5 M. J. Manos and M. G. Kanatzidis, *J. Am. Chem. Soc.*, 2012, **134**, 16441–16446.
6 X. Zhang and Y. Liu, *Environ. Sci.:Nano*, 2020, **7**, 1008–1040.
7 X. Tang, Y. Liu, M. Liu, H. Chen, P. Huang, H. Ruan, Y. Zheng, F. Yang, R. He and W. Zhu, *Nanoscale*, 2022, **14**, 6285–6290.
8 X. Li, Q. Li, W. Linghu, R. Shen, B. Zhao, L. Dong, A. Alsaedi, T. Hayat, J. Wang and J. Liu, *Environ. Technol. Innovation*, 2018, **11**, 328–338.
9 P. J. Vergamini, H. Vahrenkamp and L. F. Dahl, *J. Am. Chem. Soc.*, 1971, **93**, 6327–6329.
10 K. Patra, W. W. Brennessel and E. M. Matson, *Chem. Commun.*, 2024, **60**, 530–533.
11 K. Patra, W. W. Brennessel and E. M. Matson, *J. Am. Chem. Soc.*, 2024, **146**, 20147–20157.
12 M. Sasaki, G. Sakane, T. Ouchim and T. Shibahara, *J. Cluster Sci.*, 1998, **9**, 25–43.
13 H. Akashi, T. Shibahara and H. Kuroya, *Polyhedron*, 1990, **9**, 1671–1676.
14 R. Hernández-Molina and A. Geoffrey Sykes, *J. Chem. Soc., Dalton Trans.*, 1999, 3137–3148.
15 T. Shibahara, *Adv. Inorg. Chem.*, 1991, **37**, 143–173.
16 M. Hidai, S. Kuwata and Y. Mizobe, *Acc. Chem. Res.*, 2000, **33**, 46–52.
17 R. Llusar and S. Uriel, *Eur. J. Inorg. Chem.*, 2003, **2003**, 1271–1290.
18 B. P. Warner, B. L. Scott and C. J. Burns, *Angew. Chem., Int. Ed.*, 1998, **37**, 959–960.
19 G. te Velde, F. M. Bickelhaupt, E. J. Baerends, C. Fonseca Guerra, S. J. A. van Gisbergen, J. G. Snijders and T. Ziegler, *J. Comput. Chem.*, 2001, **22**, 931–967.
20 ADF 2019.3, SCM, Theoretical Chemistry, Vrije Universiteit, Amsterdam, The Netherlands, **https://www.scm.com**; .
21 J. P. Perdew, K. Burke and M. Ernzerhof, *Phys. Rev. Lett.*, 1996, **77**, 3865–3868.
22 J. P. Perdew, K. Burke and M. Ernzerhof, *Phys. Rev. Lett.*, 1997, **78**, 1396–1396.
23 E. van Lenthe, E. J. Baerends and J. G. Snijders, *J. Chem. Phys.*, 1994, **101**, 9783–9792.
24 S. Grimme, J. Antony, S. Ehrlich and H. Krieg, *J. Chem. Phys.*, 2010, **132**, 154104.
25 C. C. Pye and T. Ziegler, *Theor. Chem. Acc.*, 1999, **101**, 396–408.
26 A. Klamt and G. Schüürmann, *J. Chem. Soc., Perkin Trans. 2*, 1993, 799–805.
27 C. Adamo and V. Barone, *J. Chem. Phys.*, 1999, **110**, 6158–6170.
28 *Organic Electrochemistry: Revised and Expanded (5th Edition)*, ed. O. Hammerich and B. Speiser, CRC Press, 2015.
29 V. V. Pavlishchuk and A. W. Addison, *Inorg. Chim. Acta*, 2000, **298**, 97–102.
30 G. Li Manni, I. F. Galván, A. Alavi, F. Aleotti, F. Aquilante, J. Autschbach, D. Avagliano, A. Baiardi, J. J. Bao, S. Battaglia, L. Birnoschi, A. Blanco-González, S. I. Bokarev, R. Broer, R. Cacciari, P. B. Calio, R. K. Carlson, R. Carvalho Couto, L. Cerdán, L. F. Chibotaru, N. F. Chilton, J. R. Church, I. Conti, S. Coriani, J. Cuéllar-Zuquin, R. E. Daoud, N. Dattani, P. Decleva, C. de Graaf, M. G. Delcey, L. De Vico, W. Dobrautz, S. S. Dong, R. Feng, N. Ferré, M. Filatov (Gulak), L. Gagliardi, M. Garavelli, L. González, Y. Guan, M. Guo, M. R. Hennefarth, M. R. Hermes, C. E. Hoyer, M. Huix-Rotllant, V. K. Jaiswal, A. Kaiser, D. S. Kaliakin, M. Khamesian, D. S. King, V. Kochetov, M. Krośnicki, A. A. Kumaar, E. D. Larsson, S. Lehtola, M.-B. Lepetit, H. Lischka, P. López Ríos, M. Lundberg, D. Ma, S. Mai, P. Marquetand, I. C. D. Merritt, F. Montorsi, M. Mörchen, A. Nenov, V. H. A. Nguyen, Y. Nishimoto, M. S. Oakley, M. Olivucci, M. Oppel, D. Padula, R. Pandharkar, Q. M. Phung, F. Plasser, G. Raggi, E. Rebolini, M. Reiher, I. Rivalta, D. Roca-Sanjuán, T. Romig, A. A. Safari, A. Sánchez-Mansilla, A. M. Sand, I. Schapiro, T. R. Scott, J. Segarra-Martí, F. Segatta, D.-C. Sergentu, P. Sharma, R. Shepard, Y. Shu, J. K. Staab, T. P. Straatsma, L. K. Sørensen, B. N. C. Tenorio, D. G. Truhlar, L. Ungur, M. Vacher, V. Veryazov, T. A. Voß, O. Weser, D. Wu, X. Yang, D. Yarkony, C. Zhou, J. P. Zobel and R. Lindh, *J. Chem. Theory Comput.*, 2023, **19**, 6933–6991.
31 K. Andersson, P. A. Malmqvist, B. O. Roos, A. J. Sadlej and K. Wolinski, *J. Phys. Chem.*, 1990, **94**, 5483–5488.
32 K. Andersson, P. Malmqvist and B. O. Roos, *J. Chem. Phys.*, 1992, **96**, 1218–1226.
33 G. Ghigo, B. O. Roos and P. Åke Malmqvist, *Chem. Phys. Lett.*, 2004, **396**, 142–149.
34 N. Forsberg and P. Åke Malmqvist, *Chem. Phys. Lett.*, 1997, **274**, 196–204.
35 M. Douglas and N. M. Kroll, *Ann. Phys.*, 1974, **82**, 89–155.
36 B. A. Hess, *Phys. Rev. A*, 1986, **33**, 3742–3748.
37 B. O. Roos, V. Veryazov and P.-O. Widmark, *Theor. Chem. Acc.*, 2004, **111**, 345–351.
38 B. O. Roos, R. Lindh, P.-k. Malmqvist, V. Veryazov and P.-O. Widmark, *J. Phys. Chem. A*, 2005, **109**, 6575–6579.
39 F. Aquilante, T. B. Pedersen, V. Veryazov and R. Lindh, *Wiley Interdiscip. Rev.:Comput. Mol. Sci.*, 2013, **3**, 143–149.
40 G. Li Manni, R. K. Carlson, S. Luo, D. Ma, J. Olsen, D. G. Truhlar and L. Gagliardi, *J. Chem. Theory Comput.*, 2014, **10**, 3669–3680.
41 Y. Ohki, R. Hara, K. Munakata, M. Tada, T. Takayama, Y. Sakai and R. E. Cramer, *Inorg. Chem.*, 2019, **58**, 5230–5240.

42 J. Enemark and R. Feltham, *Coord. Chem. Rev.*, 1974, **13**, 339–406.
43 Y. Ohki, K. Uchida, R. Hara, M. Kachi, M. Fujisawa, M. Tada, Y. Sakai and W. M. C. Sameera, *Chem. – Eur. J.*, 2018, **24**, 17138–17147.
44 G. Li Manni, A. L. Dzubak, A. Mulla, D. W. Brogden, J. F. Berry and L. Gagliardi, *Chem. – Eur. J.*, 2012, **18**, 1737–1749.
45 C. A. P. Goodwin, M. T. Janicke, B. L. Scott and A. J. Gaunt, *J. Am. Chem. Soc.*, 2021, **143**, 20680–20696.
46 L. R. Avens, S. G. Bott, D. L. Clark, A. P. Sattelberger, J. G. Watkin and B. D. Zwick, *Inorg. Chem.*, 1994, **33**, 2248–2256.
47 S. Kihara, Z. Yoshida, H. Aoyagi, K. Maeda, O. Shirai, Y. Kitatsuji and Y. Yoshida, *Pure Appl. Chem.*, 1999, **71**, 1771–1807.
48 R. G. Pearson, *Inorg. Chem.*, 1988, **27**, 734–740.
49 S. R. Chowdhury, C. A. P. Goodwin and B. Vlaisavljevich, *Chem. Sci.*, 2024, **15**, 1810–1819.
50 Q.-R. Huang, J. R. Kingham and N. Kaltsoyannis, *Dalton Trans.*, 2015, **44**, 2554–2566.
51 G. Gervasio, R. Bianchi and D. Marabello, *Chem. Phys. Lett.*, 2004, **387**, 481–484.
52 M. Autillo, M. A. Islam, J. Jung, J. Pilmé, N. Galland, L. Guerin, P. Moisy, C. Berthon, C. Tamain and H. Bolvin, *Phys. Chem. Chem. Phys.*, 2020, **22**, 14293–14308.